CHEMISTRY OF MATERIALS

pubs.acs.org/cm

Article

Structurally Frustrated Remeika Phases: Tolerance Factor and Non-Kramers' Ion Effects

Published as part of Chemistry of Materials special issue "Honoring the Outstanding Contributions of Mercouri Kanatzidis to Chemistry of Materials".

Alexis Dominguez Montero, Gregory T. McCandless, Zachary J. Morgan, Benny Schundelmier, Christina M. Hoffmann, Ryan E. Baumbach, and Julia Y. Chan*

Cite This: *Chem. Mater.* 2025, 37, 9014−9024

Read Online

ACCESS | Metrics & More | Article Recommendations | Supporting Information

ABSTRACT: Quantum materials that are found on the verge of structural, magnetic, and electronic instabilities are deep reservoirs for exotic phenomena. Our criteria to study the reported $Ln_5Ru_6Sn_{18}$ (Ln = Gd, Tb) are guided by the tolerance factor for Remeika phases—a class of intermetallic compounds with the general formula $A_3M_4X_{13}$ (where A = rare-earth element, M = transition metal, and X = tetrel), which can be viewed as structural analogues of pseudoperovskites ($4 \times ABX_3$), with one of the tetrel atoms occupying the A-site. We have grown single crystals, up to 0.5 cm on the largest facet, of $Gd_5Ru_6Sn_{18}$ (a = 13.8052(12) Å) and $Tb_5Ru_6Sn_{18}$ (a = 13.7825(9) Å), which we expect to be on the verge of a formation instability. Bulk magnetic, heat capacity, and electrical transport measurements reveal unusual behavior that originates from the trivalent Gd and Tb ions, with deviations from typical metallic behavior and magnetic ordering that is short-range or disrupted in some other way. To better understand these phenomena, single-crystal neutron diffraction is investigated, which reveals short-range correlations among the partially occupied Tb and Sn sublattices, with 3D-ΔPDF analysis supporting direction-dependent local order. Taken together, these measurements show the utility of using tolerance factors in identifying materials that are likely to exhibit complex phenomena and uncover environments where a formation instability may strongly impact emergent bulk magnetic and electronic phenomena.

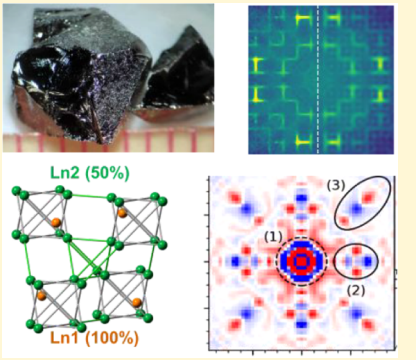

1. INTRODUCTION

Materials on the verge of structural instability often exhibit competing ground states, which can serve as a gateway to emergent and exotic ground states.[1,2] These include phenomena such as spin-liquid-like behavior,[3] structural phase transitions driven by charge density waves,[4,5] and valence instability.[6] To guide the discoveries of such materials, we have recently developed structure−property maps that enable the identification of structure types likely to host phase instabilities and strong electronic correlations, thereby facilitating the discovery of candidate systems for in-depth physical property studies.[7−9] This approach allows us to rationally prioritize synthetic targets that are both chemically accessible and physically compelling. To explore this approach, we focus on Remeika phases,[10] which encompass a large number of chemical combinations and structural variants.

The Remeika phases exhibit seven distinct structure types, including the $Yb_3Rh_4Sn_{13}$, $Er_5Rh_6Sn_{18}$, and $Tb_5Rh_6Sn_{18}$ cases.[11] The cubic $Yb_3Rh_4Sn_{13}$ structure type, with the formula $A_3M_4X_{13}$ (A = alkaline earth, lanthanides, actinides, Sc, Y; M = Group 8−10 transition metals; X = In, Si, Ge, Sn, Pb), are denoted as Phase I. These adopt a primitive cubic unit cell ($Pm\bar{3}n$) consisting of corner-sharing transition metal-centered $[MX_6]$ trigonal prisms in a 3D network forming two voids, where the $[AX_{12}]$ cuboctahedral void is filled by the most electropositive element, and the $[X_1X_{12}]$ icosahedral void is filled by the main group element, as shown in Figure 1. The sublattice consisting of the A element and the main group element filling the icosahedral void resembles that of the A15 superconductors.[12] Also, due to its structural resemblance, the cubic Phase I $Yb_3Rh_4Sn_{13}$ structure type is sometimes referred to as a pseudoperovskite, $(SnYb_3)Rh_4Sn_{12}$, where $[MX_6]$ trigonal prisms replace the transition metal-centered octahedra that are present in perovskites. The structural robustness of the $Yb_3Rh_4Sn_{13}$ structure type is underscored by the adoption of over 100 analogues with a diverse range of transition metals and main group elements,[13] resulting in a wealth of intriguing physical properties through chemical substitution with the multiple lower symmetry analogues,[14] or hettotypes, such as

Received: September 27, 2025
Revised: October 24, 2025
Accepted: October 27, 2025
Published: November 1, 2025

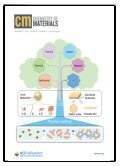

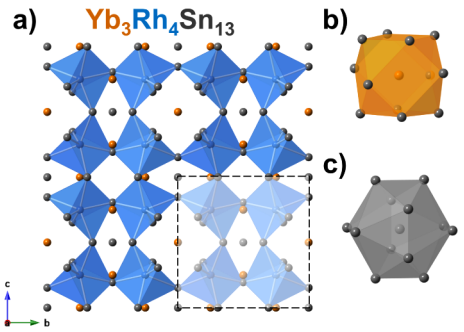

Figure 1. (a) The $Yb_3Rh_4Sn_{13}$ crystal structure is delineated by the dashed lines, with the faint area indicated. (b) Yb and (c) Sn cuboctahedral and icosahedral local environments, respectively.

the chiral $I4_132$ adopted by the Weyl–Kondo semimetal $Ce_3Rh_4Sn_{13}$,[15] the tetragonal $I4_1/amd$ adopted by the inhomogeneous mixed valence $Ce_3Ir_4Ge_{13}$,[16] and the non-centrosymmetric Cc superconductor $Y_3Pt_4Ge_{13}$.[17]

In addition, the tetragonal $Er_5Rh_6Sn_{18}$ (Figure 2) and cubic $Tb_5Rh_6Sn_{18}$ (Figure 3) with the formula $A_5M_6X_{18}$, correspond

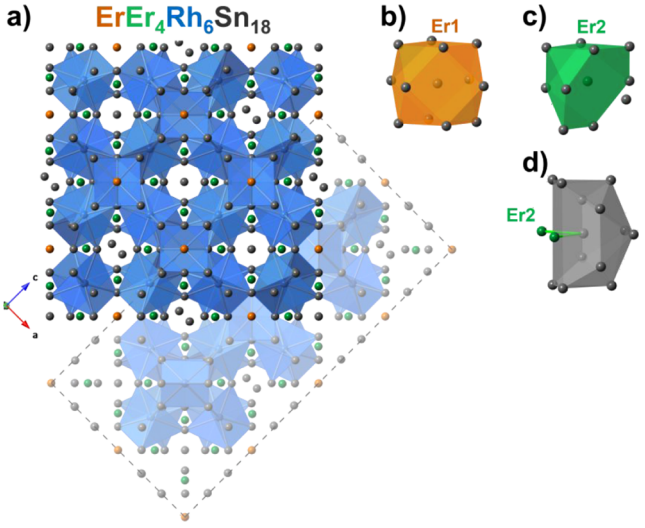

Figure 2. (a) The $Er_5Rh_6Sn_{18}$ crystal structure is delineated by the dashed lines with the faint area with Er1, 2 and Sn depicted in orange, green and gray spheres. (b–d) The local environments of Er1, 2 and Sn6 are represented in the cuboctahedron, truncated cuboctahedron and distorted icosahedron.

to Phases II and III based on Remeika's classification.[11] The tetragonal Phase II $Er_5Rh_6Sn_{18}$ also features a 3D network of corner-sharing, $[MX_6]$ transition metal-centered trigonal prisms, as shown in Figure 2. Compared to the $Yb_3Rh_4Sn_{13}$ structure type, the $Er_5Rh_6Sn_{18}$ structure type has a distinctively different arrangement of the corner-sharing trigonal prisms, resulting in two unique crystallographic sites for the A element, with A1 occupying a cuboctahedral site and A2 forming a tetrahedral arrangement with other A2 elements. A description of the structural relationship between Phases I–III is provided in the Supporting Information (Figure S1). The $A_5M_6X_{18}$ Remeika phases have garnered significant interest due to a range of intriguing phenomena, including reports of reentrant superconductivity,[18,19] unconventional superconductivity in $A_5Rh_6Sn_{18}$ (A = Sc, Y, Lu),[20−22] disorder-enhanced super-

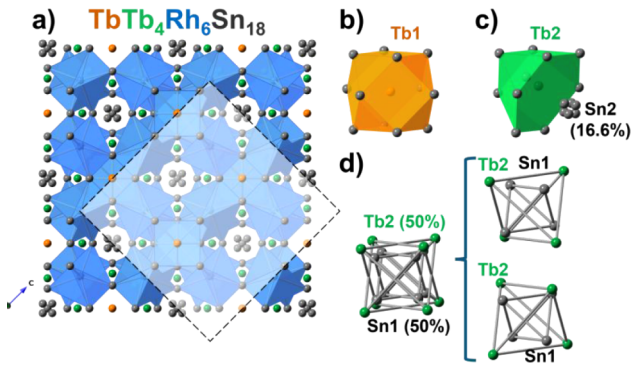

Figure 3. (a) The $Tb_5Rh_6Sn_{18}$ crystal structure is delimited by the dashed lines with the faint area with Tb1, 2 and Sn depicted in orange, green and gray spheres. (b–d) The local environments of Tb1, 2 are represented in the cuboctahedron and truncated cuboctahedron.

conductivity in $Y_5(Rh_{5-x}M_x)_6Sn_{18}$ (M = Co, Pd),[23] and the emergence of noncollinear spin structures.[24]

The tolerance factor for the Remeika phases is used to predict the stability of Phases I–III is given by $\tau = \frac{T+I}{C\sqrt{3}}$; where T, I and C represent the estimated height of the trigonal prism, the icosahedron, and cuboctahedron structural motifs, respectively, assuming close packing and ionic and covalent radii. We previously used this approach to target the synthesis of $Yb_5Ru_6Sn_{18}$ and predict the likely oxidation state of ytterbium within this structure.[10]

Herein, we report the growth of the previously reported[25] cubic Phase III $Ln_5Ru_6Sn_{18}$ (Ln = Gd, Tb) which were selected based on the following: (i) their corresponding tolerance factor values for Remeika phases (τ = 0.837 and 0.844, respectively) being near the boundary between $Yb_3Rh_4Sn_{13}$ and $Er_5Rh_6Sn_{18}$/$Tb_5Rh_6Sn_{18}$ structure types (τ = 0.83) (Figure S2), which could make them prone to structural instability that may express as disorder or a structural phase transition, (ii) the inherent tetrahedral sublattice of the lanthanides in the $Er_5Rh_6Sn_{18}$/$Tb_5Rh_6Sn_{18}$ structure types can give rise to geometric frustration, and (iii) non-Kramers' ions, such as Tb^{3+}, have a singlet ground state, allowing structural fluctuations, which in combination with disorder could further enhance quantum fluctuations through transverse interactions or fields, and potentially facilitate emergent properties.[26,27] In contrast, Gd^{3+} has a L = 0 ground state, a large magnetic moment, and minimal single-ion anisotropy, which could allow for substantial changes in magnetic entropy.

2. EXPERIMENTAL SECTION

2.1. Synthesis. $Ln_5Ru_6Sn_{18}$ (Ln = Gd, Tb) were grown by arc melting stoichiometric ratios of the raw elements, resulting in a weight loss of <3%. The boules were cut into four equivalent pieces and placed in a Canfield alumina crucible[28] with 20 additional moles of Sn. The samples were sealed inside a fused silica tube under ∼1/3 atm of argon. The resulting ampule was placed in a programmable furnace at 300 °C, heated to 1175 °C at a rate of 100 °C/h, and dwelled for 24 h. The sample was then cooled at a rate of 2 °C/h until it reached 935 °C, at which point the ampule was rapidly removed, inverted, and centrifuged. The reaction product for the Gd analogue consisted of a faceted $Gd_5Ru_6Sn_{18}$ single crystal, up to 0.4 cm on each side, with a Ru_3Sn_7 crystal ∼0.1 cm on each

https://doi.org/10.1021/acs.chemmater.5c02568
Chem. Mater. 2025, 37, 9014−9024

side. In contrast, the Tb analogue produced a faceted $Tb_5Ru_6Sn_{18}$ single crystal of 0.5 cm on its largest facet with millimeter-sized cubes of an unknown phase on its surface, which were easily removed after etching using 12.1 M HCl: H_2O in a 1:2 volume ratio. Reactions that excluded the arc melting step resulted in multiple smaller $Ln_5Ru_6Sn_{18}$ crystals, albeit with an increased proportion of Ru_3Sn_7.

2.2. Diffraction. Room temperature single crystal X-ray diffraction data was collected from single crystal shards of Gd ($0.02 \times 0.04 \times 0.04$ mm^3) and Tb ($0.04 \times 0.04 \times 0.04$ mm^3) analogues. Data was collected using a Bruker D8 Quest Kappa single-crystal X-ray diffractometer with an IμS microfocus source (Mo Kα radiation λ = 0.71073 Å) and a PHOTON III CPAD area detector. The raw data frames were processed using Bruker SAINT program, and a multiscan absorption correction method was applied using SADABS.[29] A preliminary starting model was obtained by intrinsic phasing method in SHELXT and further refined by least-squares refinement in SHELXL.[30,31]

Single crystal data refinement of $Ln_5Ru_6Sn_{18}$ (Ln = Gd, Tb) showed high residual electron density next to the Ru-centered trigonal prisms. A refinement considering two trigonal prism orientations 90° apart along the C_2 axis of the prism was modeled by reducing the site occupation factor of the Sn1 site by half. The Ln2 and Sn1 occupancies were reduced to 50%, while the Sn2 occupancies were reduced to 16.67%, respectively, by adjusting the multiplicity to the corresponding value due to unrealistic bond distances if fully occupied, with the refined formula corresponding to $Ln_5Ru_6Sn_{18}$ (Ln = Gd, Tb). The percentage assigned was determined first by refining the occupancy of the Ln2, Sn1, and Sn2, which yielded nearly 50%, 50%, and 16.67%, respectively. The values assigned to Ln2, Sn1, and Sn2 match the 3D-ΔPDF analysis discussed in Section 3.1, suggesting direction-dependent local order.

$Ln_5Ru_6Sn_{18}$ (Ln = Gd, Tb) samples were pulverized using a mortar and pestle. The powders were mounted on a low-background Si sample holder. Measurements were performed on a Bruker D2 Phaser with Cu Kα radiation (λ = 1.54184 Å) between 2θ = 5−80° with a 0.02° step size and an exposure time of 1 s per step. Rietveld refinements were performed using the CIF generated through single-crystal X-ray diffraction data. Figure S3 shows the Rietveld refinement on $Ln_5Ru_6Sn_{18}$ (Ln = Gd, Tb) experimental data. X-ray backscattering images of $Tb_5Ru_6Sn_{18}$ were acquired using a Photonic Science Laue system (AL048) coupled with a Thermo Kevex DXS-11−5025 X-ray source (W Kα radiation, λ = 0.21062 Å), and a dual-lens coupled Laue camera. The backscattering X-ray collection was performed on the flat surface of the crystal along the [100] as shown in Figure S4 to determine the quality of the single crystals.

Single crystal neutron diffraction experiments were conducted at the TOPAZ Single Crystal Diffractometer at the Spallation Neutron Source (SNS), Oak Ridge National Laboratory (ORNL).[32] Data were collected using a single crystal fragment with dimensions of $0.2 \times 0.5 \times 1$ mm^3, which was glued to a 1 mm diameter Kapton loop on a pin secured in a magnetic MiTeGen base. The base was then transferred to the TOPAZ instrument and attached to a two axis, ambient goniometer from Crystal Logic Inc., equipped with a Cobra 800+ liquid nitrogen cryostream from Oxford Cryosystems, capable of controlling the sample temperature between 90 K−500 K. The sample was centered with point-and-click online centering software implemented in the *EPICS* data collection software. The unit cell dimensions, and sample orientation were determined from the first randomly oriented neutron data using the *Mantid* data analysis package.[33]

This information was used to find the data collection strategy to cover a full sphere of reciprocal space. For the data acquisition strategy, the *CrystalPlan* software[34] was used. The TOPAZ instrument is a high-resolution, wavelength-resolved, time-of-flight Laue single crystal neutron diffractometer covering a wavelength band of roughly 3 Å, from 0.4 Å to 3.5 Å. This allows for the collection of data at a series of individual, fixed crystal orientations, where each covers a volume of reciprocal space, captured in 24 positions and wavelength sensitive neutron detectors. Blank spaces between detectors after each orientation are filled in by rotating the sample the appropriate angles around omega and phi of the goniometer to the next position, and collecting data until the required unique volume of reciprocal space is covered to provide a complete sphere for data analysis. For the $Tb_5Ru_6Sn_{18}$ sample, 9 orientations were collected at 100 K and at 293 K each.

Data collection was optimized for maximal reciprocal space coverage and used three omega settings (0°, 25°, and 50°) and phi rotations in 60° increments from −180° to +180°, with a fixed chi offset of 45°. This provided complete volumetric reciprocal space coverage, which is necessary to analyze diffuse scattering signals. Each orientation was measured for a total proton charge of 6 Coulomb, corresponding to approximately 1.25 h per setting.

All data were combined into a contiguous reciprocal space volume of high resolution, covering $h, k, l \pm 15$. Data were corrected for sample specific contributions (absorption, neutron path length, Lorenz factor) and instrument specific contributions (incident flux, detector efficiency), using the isotropic incoherent scattering of a niobium doped vanadium sphere; this included normalization and scaling.[33,35] Background was subtracted using a no-sample reference measurement. Symmetry averaging was applied using the Laue point group $m\bar{3}m$.

To prepare the diffuse scattering pattern for 3D delta PDF analysis, Bragg peaks were removed from the data volume using small regions of interest (ROIs) centered on each reflection. The removed regions were backfilled by Gaussian-smoothing interpolation of the surrounding background.

2.3. Magnetic Susceptibility and Magnetization. Magnetic properties were measured on an arbitrarily oriented $Ln_5Ru_6Sn_{18}$ (Ln = Gd, Tb) single crystals of 4.3 and 34.7 mg, respectively, using a Magnetic Properties Measurement System (MPMS). Temperature-dependent magnetic susceptibility ($\chi = M/H$) was measured from 1.8−300 K under an applied magnetic field of H = 0.1 T (ZFC) and field-cooled (FC) conditions. Field-dependent magnetization isotherms (M/H) were measured at 1.8 K for -7 T < H < 7 T.

2.4. Electrical Resistivity. A Physical Properties Measurement System (PPMS) was used to measure the temperature-dependent electrical resistivity $\rho(T)$ in a zero magnetic field. $\rho(T)$ was measured between 1.8−300 K, respectively. $\rho(T)$ measurements were performed using the four-wire method, where platinum wires were spot-welded to the sample.

3. RESULTS AND DISCUSSION

3.1. Structure. $Ln_5Ru_6Sn_{18}$ (Ln = Gd, Tb) adopt the cubic Phase III $Fm\bar{3}m$ $Tb_5Rh_6Sn_{18}$ structure type with a = 13.8052(12) Å and 13.7825(9) Å, respectively. The crystallo-

https://doi.org/10.1021/acs.chemmater.5c02568
Chem. Mater. 2025, 37, 9014−9024

graphic data refinement and atomic coordinates are provided in Tables 1, 2, and 3. The $Ln_5Ru_6Sn_{18}$ (Ln = Gd, Tb)

Table 1. Crystallographic Data and Refinement Parameters of $Ln_5Ru_6Sn_{18}$ (Ln = Gd, Tb)

Empirical Formula	$Gd_5Ru_6Sn_{18}$	$Tb_5Ru_6Sn_{18}$
Space group	$Fm\bar{3}m$	$Fm\bar{3}m$
Lattice parameters, a [Å]	13.8052(12)	13.7825(9)
Volume [Å^3]	2631.0(7)	2618.1(5)
Z	4	4
Density [g/cm^3]	8.909	8.975
Absorption coefficient [mm^{-1}]	32.43	33.43
$F(000)$	5936	5956
Radiation and wavelength, λ [Å]	Mo Kα, 0.71073	Mo Kα, 0.71073
Temperature [K]	298	298
Crystal size [mm^3]	0.02 × 0.04 × 0.04	0.04 × 0.04 × 0.04
θ range [°]	2.6−30.5	2.6−30.5
Index range		
h	−19 → 19	−19 → 19
k	−19 → 19	−19 → 19
l	−19 → 19	−19 → 19
Number of reflections	32455	32141
Unique reflections	248	246
Data/restraints/parameters	248/0/20	246/0/20
R_{int}	0.097	0.070
$\Delta\rho_{max/min}$ [eÅ^3]	2.53/−1.62	1.81/−0.87
GoF	1.40	1.18
R_1 [$F^2 > 2\sigma(F^2)$]	0.023	0.015
wR_2 (F^2)	0.057	0.035

structure, as shown in Figure 4a, consists of two Ln, one Ru, and three Sn crystallographically distinct sites and can be understood as a cubic average structure of the $Er_5Rh_6Sn_{18}$ structure type (Figure 2). To facilitate the description of the $Ln_5Ru_6Sn_{18}$ (Ln = Gd, Tb) analogues, we will first describe the Phase II $Er_5Rh_6Sn_{18}$ structure type. The $Er_5Rh_6Sn_{18}$ structure type consists of a 3D network of two crystallographically distinct, corner-sharing [$RhSn_6$] trigonal prisms.[36] The Rh1-centered trigonal prism consists of six Sn atoms (two Sn1, two Sn5, and two Sn6), while the Rh2-centered trigonal prism consists of Sn3−6 atoms (one of each), and two Sn1. Er1 (Figure 2b) resides in a cuboctahedral local environment consisting of 12 Sn atoms (two Sn3, two Sn4, four Sn5, four Sn6), which are face-sharing on all six quadrilateral faces with six trigonal prisms (two Rh1 and four Rh2 centered). The two Sn1 sites of each trigonal prism are corner-sharing with five more [$RhSn_6$] trigonal prisms forming an [Sn_4] isotetrahedron as depicted in Figure S5. The Er2 local environment resembles that of a truncated cuboctahedron (or triangular cupola) (Figure 2c) and has a tetrahedral arrangement with respect to other Er2 sites, interpenetrating the [Sn_4] tetrahedron formed by Sn1 (Figure S6). This motif is also present in $Sm_2Ru_3Sn_5$,[37] a ternary ordered variant of the Ru_3Sn_7 structure type. The Sn2 resides in an irregular polyhedron that consists of 14 vertices (two Er2, two Sn2, two Sn4, two Sn5, four Sn6, and two Sn1), as shown in Figure 2d. The Er2 tetrahedra arrangement with respect to the Sn2 site is emphasized in Figure S6c. The alternating arrangement between cuboctahedral and [Sn_4] tetrahedra voids formed by the corner-sharing trigonal prisms occurs in all 3D, contrary to the $Yb_3Rh_4Sn_{13}$ structure type, where it only occurs in 2D, resulting instead in face-sharing cuboctahedra and icosahedral structural motif instead of the irregular 14 vertices polyhedron (see Supporting Information for more details).

The $Ln_5Ru_6Sn_{18}$ (Ln = Gd, Tb) (Figure 3) in the $Tb_5Rh_6Sn_{18}$ structure type features a single type of Ru-centered trigonal prism. This prism can adopt two distinct orientations, determined by the specific pair of nonadjacent Sn1 sites that are occupied (Figure 4b and c). As observed in the tetragonal $Er_5Rh_6Sn_{18}$ structure type, the Ln1 site in $Ln_5Ru_6Sn_{18}$ is coordinated in a cuboctahedral environment composed of 12 Sn3 sites. This cuboctahedral shares all six of its square faces with six neighboring Ru-centered trigonal prisms, as illustrated in Figure 5a. On the other hand, each pair of nonadjacent Sn1 sites of the trigonal prism is corner-sharing with the pair of Sn1 of five more [$RhSn_6$] trigonal prisms forming a [Sn_4] regular tetrahedron of Sn1, as depicted in Figure 5b and c. The Ln2 local environment resembles that of a truncated cuboctahedron and has a regular tetrahedral arrangement with respect to other Ln2 sites (Figure 3c), interpenetrating the [Sn_4] tetrahedron formed by Sn1 (Figure 3d). Due to the distinct possible nonadjacent pairs of Sn1, there are two possible orientations for each [Sn_4] and Ln2 tetrahedra. The Sn2 resides in an irregular polyhedron that consists of 14 vertices (two Ln2, two Sn1, and 10 Sn3). The tetrahedral arrangement observed for Ln2 and Sn1 in the $Er_5Rh_6Sn_{18}$ structure type is averaged in the $Ln_5Ru_6Sn_{18}$ (Ln = Gd, Tb) (Figure 4d), with two of the six possible orientations of the Ln2 being shown in Figure 4e. The Sn2 site is 1/6 occupied and may be related to the six possible orientations that Ln2 and Sn1 could occupy (two of which are shown in Figure 4e), where the bond distance between Sn2 and Ln2 limits the possible site. Table 4 provides bond distances in the $Ln_5Ru_6Sn_{18}$ (Ln = Gd, Tb). The volumes of the [$RuSn_6$] trigonal prisms in $Ln_5Ru_6Sn_{18}$, where Ln = Gd or Tb, are 18.879 and 18.814 Å^3, respectively. These volumes are smaller than the volume found in $Sm_2Ru_3Sn_5$, which is 19.814 Å^3. Similarly, the volumes of the [Ln_4] tetrahedra in $Ln_5Ru_6Sn_{18}$ for Gd and Tb are 16.946 and 16.821 Å^3, respectively, also smaller than the volume in $Sm_2Ru_3Sn_5$, which measures 18.291 Å^3. The differences in volume among these structurally similar motifs may be attributed to the larger atomic radius of Sm compared to those of Gd and Tb. During the integration

Table 2. Fractional Atomic Coordinates and Displacement Parameters of $Gd_5Ru_6Sn_{18}$

Site Label	Symmetry	x	y	z	U_{eq} (Å^2)	Occ.
Gd1	$m\bar{3}m$	0	0	0	0.0126(4)	
Gd2	.3m	0.36584(6)	0.36584(6)	0.36584(6)	0.0107(3)	1/2
Ru1	4m.m	0.24619(9)	0	1/2	0.0078(3)	
Sn1	.3m	0.41128(8)	0.41128(8)	0.41128(8)	0.0106(4)	1/2
Sn2	2.mm	0.2140(4)	1/4	1/4	0.047(2)	1/6
Sn3	m.m2	0.82641(4)	0.82614(4)	0	0.0154(3)	

https://doi.org/10.1021/acs.chemmater.5c02568
Chem. Mater. 2025, 37, 9014−9024

Table 3. Fractional Atomic Coordinates and Displacement Parameters of $Tb_5Ru_6Sn_{18}$

Site Label	Symmetry	x	y	z	U_{eq} (Å^2)	Occ.
Tb1	$m\bar{3}m$	0	0	0	0.0125(2)	
Tb2	.3m	0.36595(3)	0.36595(3)	0.36595(3)	0.00869(16)	1/2
Ru1	4m.m	0.24600(5)	0	1/2	0.00640(16)	
Sn1	.3m	0.41150(4)	0.41150(4)	0.41150(4)	0.0095(2)	1/2
Sn2	2.mm	0.2134(2)	1/4	1/4	0.0426(13)	1/6
Sn3	m.m2	0.82608(2)	0.82608(2)	0	0.01332(14)	

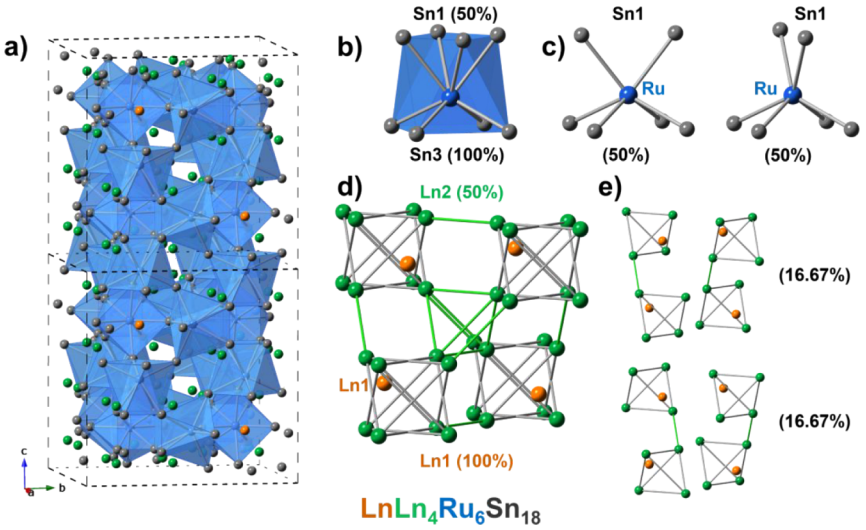

Figure 4. (a) $Ln_5Ru_6Sn_{18}$ unit cell with the origin shifted (1/2, 3/4, 1/8) to ease comparison with the $Er_5Rh_6Sn_{18}$ structure type (see Figure 2) with Ln1, Ln2, Ru, and Sn in orange, green, blue, and gray spheres, respectively. Two-unit cells are shown along the c-axis to resemble the lattice parameters of $Er_5Rh_6Sn_{18}$. The positionally disordered [$RuSn_6$] trigonal prisms and Sn1 sites, as well as the Ln2 tetrahedra, are shown, with the Sn2 site omitted. (b, c) Representation of the overlapping trigonal prism with the partially occupied (50%) Sn1 site. (d) Representation of the positionally disordered tetrahedron formed by Ln2 sites, with green lines representing the closest Ln2−Ln2 contact, and gray lines representing the overlapping Ln2 tetrahedra. For clarity, the interpenetrating Sn1 tetrahedra and Sn2 in figures (d) and (e) were omitted. (e) Two of the six possible orientations for the tetrahedra formed by Ln2, notice that the Ln1 site is unchanged between each orientation.

procedure of the single crystal X-ray diffraction data, weak diffuse scattering was observed in the precession images of both analogues, and further study was conducted only on $Tb_5Ru_6Sn_{18}$.

To investigate local structural disorder and diffuse scattering, single-crystal neutron diffraction data were analyzed using the 3D difference pair distribution function (3D-ΔPDF). For the complex structure of $Tb_5Ru_6Sn_{18}$, extracting real-space correlations is more effective due to the high number of atoms per unit cell. Reverse Monte Carlo (RMC) methods, like Spinvert or RMC-discord fit diffuse scattering data with large supercells, but need plausible starting models.[38,39] The 3D-ΔPDF technique[40] provides a model-free view of atomic pair correlations, allowing interpretation with tools like Yell software.[41]

We fitted diffuse scattering data by examining atomic bond-pair vectors within two unit cells. A unit cell expanded into a supercell revealed unique bond pairs contributing to diffuse features. Using the Laue symmetry group, we minimized the parameter space by grouping symmetry-equivalent bond pairs. The calculated diffuse intensity, formed from phase factors and fitting coefficients, was compared to experimental patterns. Iterative testing showed that only the partially occupied Tb, Sn1, and Sn2 sites were necessary to match diffuse scattering features. Figure 6 shows representative comparisons between the observed and refined patterns for reciprocal space slices through the (hk2) and (hk3) planes (panels 6a and 6b). The refinement captures the distinct diffuse features in these planes, significantly simplifying the interpretation of the 3D-ΔPDF by attributing it primarily to correlations involving these partially occupied sites. These features cannot be attributed to magnetic correlations, as the magnetic form factor suppresses scattering features further out in the reciprocal space. In contrast, neutrons scattering from atomic nuclei do not experience a momentum transfer-dependent form factor (unlike X-rays). Consequently, the rise in neutron scattering intensity at larger momentum transfer values is a hallmark of structural disorder.

A subset of the disordered atomic sites is illustrated in Figure 7a, extended beyond the first unit cell along the a- and b-axes, with a thin slab extracted along the c-axis. This perspective highlights the cluster of six partially occupied Sn2 positions and their neighboring Tb−Tb, Sn−Sn, and Tb−Sn pairs, oriented along the [100] and [110] directions. The corresponding 3D-ΔPDF is shown in Figure 7b, visualized just beyond one unit cell separation to reveal short-range correlations. A finite integration thickness is applied along the c-axis to include the slight out-of-plane components, while integration just near the origin is limited to preserve the fine structure surrounding the Sn2 cluster.

Near the origin, labeled (1) in the zoomed-in view of Figure 7b, a finite ring of negative density appears just offset from the autocorrelation peak, indicating that likely only one of the possible six Sn2 positions can be occupied. Surrounding this, a second shell of positive density is observed, including an out-

https://doi.org/10.1021/acs.chemmater.5c02568
Chem. Mater. 2025, 37, 9014−9024

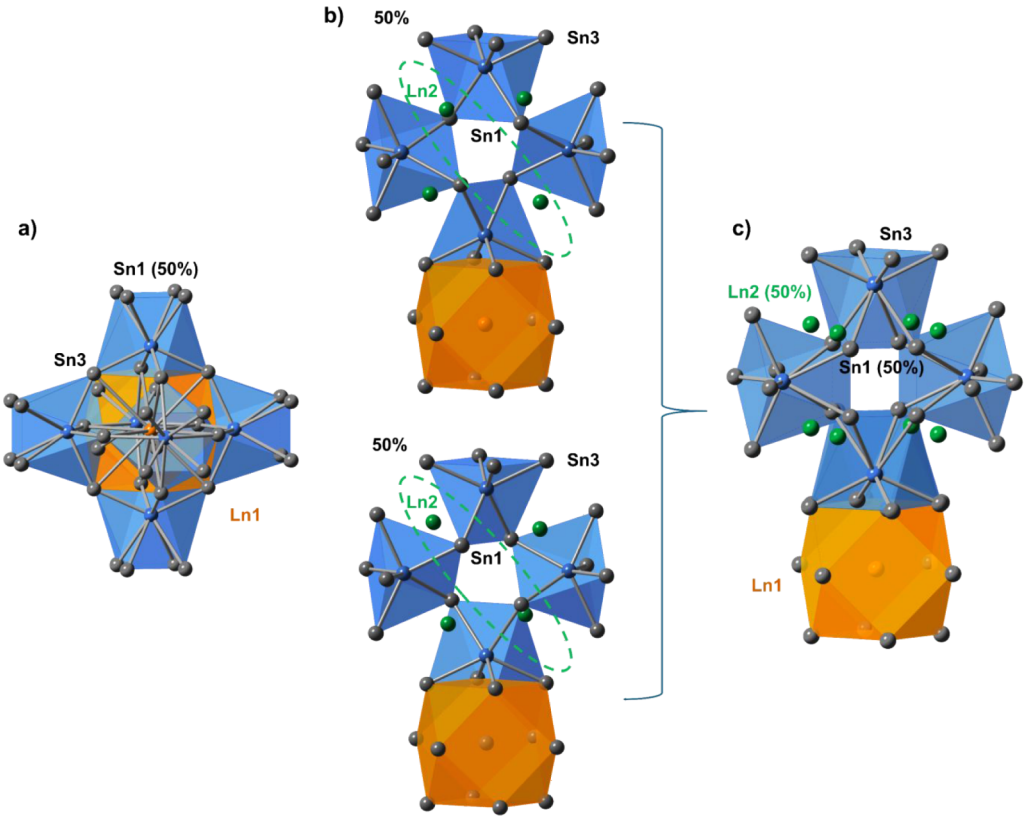

Figure 5. (a) The local environment of the [$LnSn_{12}$] cuboctahedral structural motif, featuring six face-sharing [$RuSn_6$] trigonal prisms. Ln1, Ln2, Ru, and Sn are represented by orange, green, blue, and gray spheres, respectively. (b) Both potential orientations of the six corner-sharing [$RuSn_6$] trigonal prisms (two of which are omitted for clarity). The dashed green ellipse highlights the distinct arrangement of the Sn1 and Ln2 tetrahedron. (c) The average structure of the six corner-sharing [$RuSn_6$] trigonal prisms (two of which are omitted for clarity).

Table 4. Selected Interatomic Distances (Å) in $Ln_5Ru_6Sn_{18}$ (Ln = Gd, Tb)

$Ln_5Ru_6Sn_{18}$	$Gd_5Ru_6Sn_{18}$	$Tb_5Ru_6Sn_{18}$
Ln1−Ln2 (x12)	5.6893(5)	5.6803(4)
Ln2−Ln2 (x1)	4.523(2)	4.5202(12)
Ln2−Ln2 (x3)	5.2385(12)	5.2256(6)
Ln1−Ru1 (x6)	3.5040(12)	3.5007(7)
Ln2−Ru1 (x3)	3.0418(9)	3.0344(5)
Ln2−Sn1 (x3)	3.2023(13)	3.1932(7)
Sn1−Sn1 (x3)	3.4643(16)	3.4500(8)
Ru1−Sn1 (x2)	2.7795(10)	2.7727(6)
Ru1−Sn3 (x4)	2.6418(6)	2.6389(4)

of-plane component. This region corresponds to the nearest-neighbor Tb−Sn1 separation. This suggests a preferred pairing between occupied Sn1 sites to nearby Tb atoms. At greater distances, strongly negative lobes emerge, extending from the Tb atoms toward adjacent Sn2 sites at the boundary of the cluster. These features might imply that an occupied Tb site suppresses nearby Sn2 occupancy, favoring configurations where Sn2 atoms are positioned farther away.

Along the [100] direction, labeled (2) in the zoomed-in view of Figure 7b, neighboring Tb−Tb and Sn1−Sn1 sites are associated with negative ΔPDF peaks, suggesting nearby exclusion. However, a positive peak appears just above and between them, originating from the Tb−Sn1 bond, with slight extensions along the [010] and [001] directions. This indicates residual correlation between Tb and Sn1 atoms near their respective neighbors. By contrast, along the [110] direction, labeled (3), occupied Sn1 or Tb sites exhibit positive correlations with like atom types at nearby positions—evident from the paired positive peaks within the marked ellipse. Meanwhile, a negative peak appears from the out-of-plane Tb−Sn1 bond, highlighting the direction-dependent nature of the correlations.

These correlations extend beyond the nearest neighbor shell. For example, along the bond vector (4) in the [100] direction one unit cell away, Tb−Tb and Sn1−Sn1 show positive correlations, while the intervening Tb−Sn1 bond is negatively correlated, forming a symmetric four-peak motif. By contrast, along bond vector (5) in the [110] direction halfway across the unit cell, the pattern is reversed: Tb−Tb and Sn1−Sn1 show negative correlations, while Tb−Sn1 is positively correlated.

Taken together, these observations reveal a complex, direction-dependent correlation network, with distinct behavior along [100] and [110] directions—potentially influenced by the presence of Sn2 atoms along [110]. These features support a configurational landscape of Tb2 tetrahedra that goes beyond the average structure and may explain the enhanced magnetic fluctuations discussed in Section 3.2.

The anisotropic short-range order and competing interactions motivate additional theoretical modeling that captures the configurational energy and directional preferences of the partially occupied Tb and Sn sublattices. Future work incorporating cluster expansion or Monte Carlo simulations could provide a quantitative framework for understanding the underlying energetic landscape driving this directional disorder.

https://doi.org/10.1021/acs.chemmater.5c02568
Chem. Mater. 2025, 37, 9014−9024

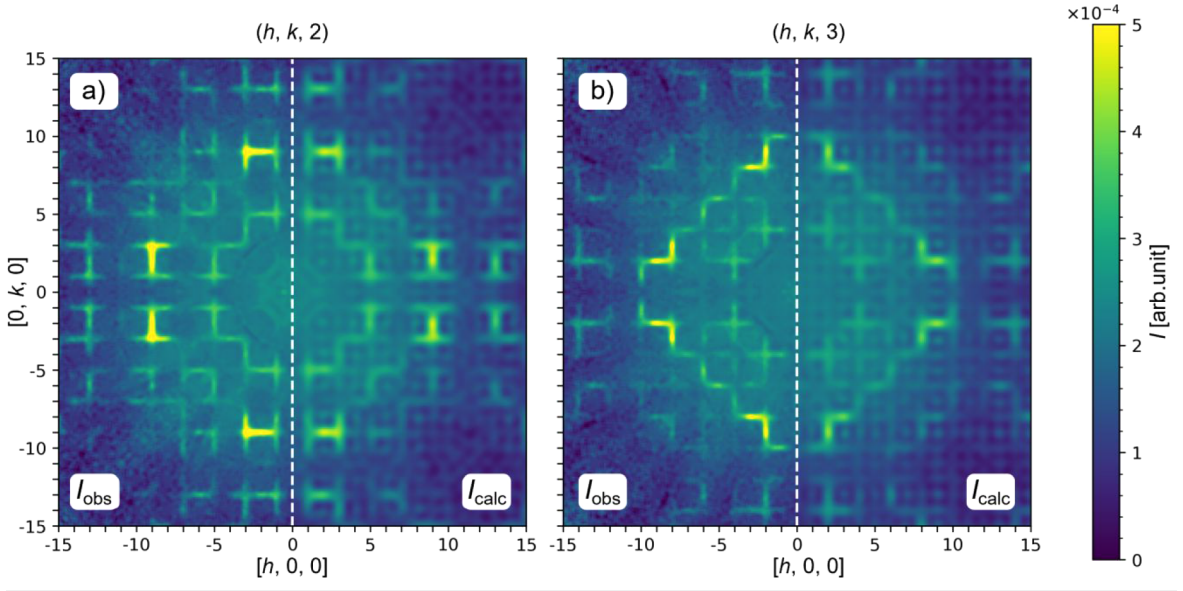

Figure 6. Single-crystal diffuse neutron scattering from $Tb_5Ru_6Sn_{18}$ at T = 300 K, showing reciprocal space slices through (a) the ($hk2$) and (b) the ($hk3$) planes. Prominent diffuse features extend beyond 15 reciprocal lattice units. For each slice, the observed intensity (left) is compared to the calculated intensity (right) from the diffuse scattering refinement. The model, which includes only the partially occupied Tb and Sn sites, successfully captures the subtle features observed in the experimental data.

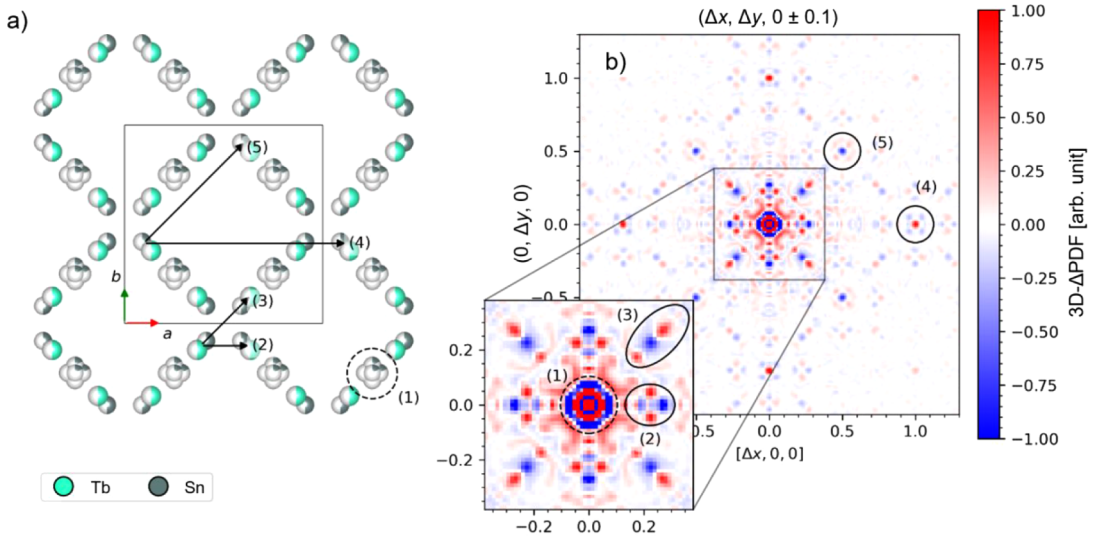

Figure 7. (a) A schematic of the average structure highlighting the partially occupied Tb and Sn sites within the *ab*-plane and the first quarter along the *c*-axis. The large, central square denotes the first unit cell. Selected Tb−Sn bond vectors are illustrated and enumerated in order of increasing distance along the [100] and [110] directions. Label (1) marks a small cluster of six Sn2 atom sites and nearest neighbor Tb−Sn1 bonds. Labels (2) and (4) indicate [100]-type Tb−Tb and Sn−Sn bonds at approximately 0.25 and exactly 1 unit cell separation, respectively. Labels (3) and (5) denote Tb−Tb and Sn−Sn bonds at approximately 0.25 and 0.5 unit cell shifts along [110], respectively. (b) The 3D delta-PDF derived from the diffuse scattering data, shown with an arbitrary scale to emphasize positive (red) and negative (blue) correlations. Except very near the origin, a finite thickness of ± 0.1 fractional coordinates along z is integrated to capture out-of-plane Tb−Sn correlations, complementing the in-plane Tb−Tb and Sn−Sn correlations confined to Δz = 0. The inset provides a zoomed-in view of the nearest-neighbor correlations labeled (1−3).

3.2. Magnetic Susceptibility and Magnetization.

Figure 8 shows the temperature-dependent magnetic susceptibility with H = 0.1 T applied for arbitrarily oriented $Ln_5Ru_6Sn_{18}$ (Ln = Gd, Tb) single crystals. The Curie−Weiss fit ($1/\chi = (T - \theta_{CW})/C$) between 200−300 K range (Figure 8 inset) yields Curie−Weiss constants (θ_{CW}) of −20.02 and −9.95 K for the Gd and Tb analogues, respectively. The negative values for θ_{CW} suggest dominant antiferromagnetic interactions in the paramagnetic regime for both analogues.

Using the formula $\mu_{eff} = \sqrt{8C}$, where C is normalized to the five lanthanides per formula unit, the effective magnetic moments (μ_{eff}) were calculated to be 7.79 and 9.98 μ_B/Ln, respectively. The values obtained are close to the expected 7.94 and 9.72 μ_B/Ln Hund's rule values for Gd^{3+} and Tb^{3+}, respectively. No magnetic ordering was observed down to 1.8 K. However, a weak but noticeable change in the inverse slope of the magnetic susceptibility was observed around 6 K for both compounds, with the effect being more pronounced in the Gd analogue, as shown in the inset of Figure 11. Given the

https://doi.org/10.1021/acs.chemmater.5c02568
Chem. Mater. 2025, 37, 9014−9024

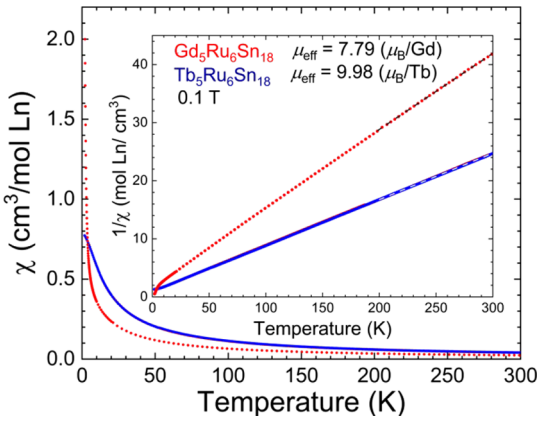

Figure 8. Magnetic susceptibility of $Ln_5Ru_6Sn_{18}$ (Ln = Gd, Tb) as a function of temperature under 0.1 T. The inset shows the inverse magnetic susceptibility with the corresponding Curie−Weiss fit, represented by dashed lines.

appreciable θ_{CW} values, the lack of long-range magnetic ordering is unexpected. But similar to $Gd_5Ru_6Sn_{18}$, the $Gd_5Os_6Sn_{18}$ and $Dy_5Os_6Sn_{18}$, which also adopt the cubic $Tb_5Rh_6Sn_{18}$ structure type and have a Kramers' ion, showed no sign of long-range magnetic ordering down to 70 mK.[18] However, the isostructural non-Kramers' ion analogues, $Tb_5Os_6Sn_{18}$ and $Ho_5Os_6Sn_{18}$, superconduct at 1.4 K.[18] Therefore, the lack of long-range magnetic ordering could be intrinsic to the structural disorder observed in the $Tb_5Rh_6Sn_{18}$ structure type analogues, including the $Ln_5Ru_6Sn_{18}$ (Ln = Gd, Tb).

In the case of $Tb_5Ru_6Sn_{18}$, the short-range antiferromagnetic correlations inferred from magnetization and heat capacity (Section 3.4) are consistent with the spatially extended, but anisotropic local order revealed by neutron 3D-ΔPDF analysis. In particular, the complex ordering among nearby Tb and Sn sites may limit cooperative magnetic ordering and promote additional magnetic frustration.

As shown in Figure 9, the field-dependent isothermal magnetization M(H) of $Gd_5Ru_6Sn_{18}$ reaches 5.1 and 4.8 μ_B/Gd at 1.8 and 5 K, respectively, under 7 T, while $Tb_5Ru_6Sn_{18}$ reaches 5.3 μ_B/Tb at 1.8. The reduced magnetic saturation (M_s) for the Tb analogue at 1.8 K could be due to crystal

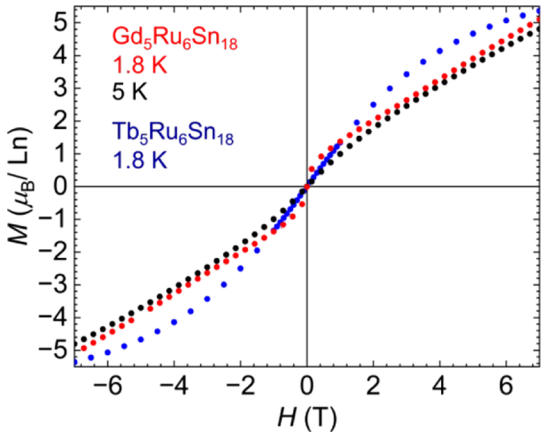

Figure 9. Magnetization as a function of applied field at 1.8 K (red and blue) and 5 K (black) from −7 to 7 T of $Ln_5Ru_6Sn_{18}$ (Ln = Gd, Tb).

electric field splitting of the Hund's rule multiplet while the origin of the reduced M_s under 7 T for $Gd_5Ru_6Sn_{18}$ (where the orbital angular momentum $L = 0$) is less clear and may indicate that larger magnetic fields will drive a metamagnetic phase transition to recover the full saturation moment.

3.3. Electrical Resistivity. The temperature-dependent electrical resistivity, $\rho(T)$, between 1.8 and 300 K of $Ln_5Ru_6Sn_{18}$ (Ln = Gd, Tb), is shown in Figure 10. Both

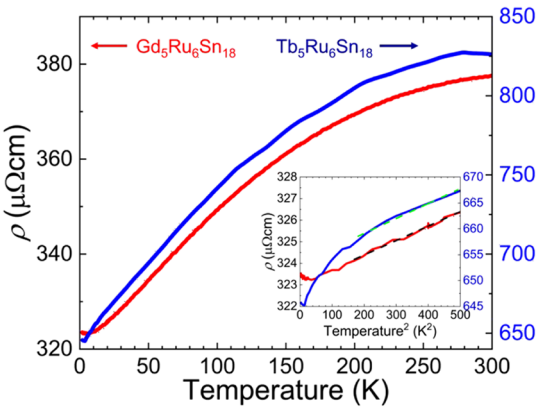

Figure 10. Temperature-dependent resistivity of $Gd_5Ru_6Sn_{18}$ (left y-axis) and $Tb_5Ru_6Sn_{18}$ (right y-axis, in blue). A slight upturn in resistivity is observed near 5 K for both compounds. The inset shows the resistivity plotted against T^2, highlighting the linear fits in the low-temperature regime up to 500 K^2.

compounds exhibit a weak decrease in electrical resistivity with temperature, consistent with metallic behavior. However, both compounds also exhibit large residual resistivities, indicating strong disorder scattering of the conduction electrons. A slight upturn below 5 K is observed in $\rho(T)$ of both analogues, which coincides with a change of slope in the inverse magnetic susceptibility, suggesting either spin scattering effects, a change in the Fermi surface caused either by the magnetic periodicity being larger than the lattice periodicity, superzone gap,[42] or a spin reorientation. The temperature dependence of electrical resistivity plotted as a function of temperature squared (T^2) between 3−500 K^2 for $Ln_5Ru_6Sn_{18}$ (Ln = Gd, Tb) is shown in the inset of Figure 8. A linear fit in the range 150−500 K^2, using the expression $\rho(T) = \rho_0 + AT^2$, characteristic fit used to describe a Fermi liquid, is applied to both compounds. The fits are represented by black and green dashed lines for the Gd and Tb analogues, respectively. The resulting parameters are ρ_0 = 323.05 μΩ cm and A = 0.0067 μΩ cm/K^2 for Gd and ρ_0 = 653.35 μΩ cm and A = 0.0288 μΩ cm/K^2 for Tb analogues. Deviation from linearity is observed for the Tb analogue below 150 K^2.

3.4. Heat Capacity. Heat capacity measurements (C_p) were collected down to 1.8 K under zero-field conditions for both the Gd and Tb analogues. Typical phonon-dominated behavior is seen for temperatures above 50 K, while the influence of magnetic degrees of freedom is seen at lower temperatures. The C_p vs T for $Gd_5Ru_6Sn_{18}$ peaks at 3.6 K, while $Tb_5Ru_6Sn_{18}$ shows a broad feature with a maximum around 6 K (Figure 11). The lambda-shaped peak in C_p vs T observed for $Gd_5Ru_6Sn_{18}$ coincides with a change in the slope of the inverse magnetic susceptibility (inset in Figure 11, red) and, therefore, suggests a common origin. Similarly, the broad feature observed in C_p vs T observed for $Tb_5Ru_6Sn_{18}$ coincides with a change in the slope of the inverse magnetic

https://doi.org/10.1021/acs.chemmater.5c02568
Chem. Mater. 2025, 37, 9014−9024

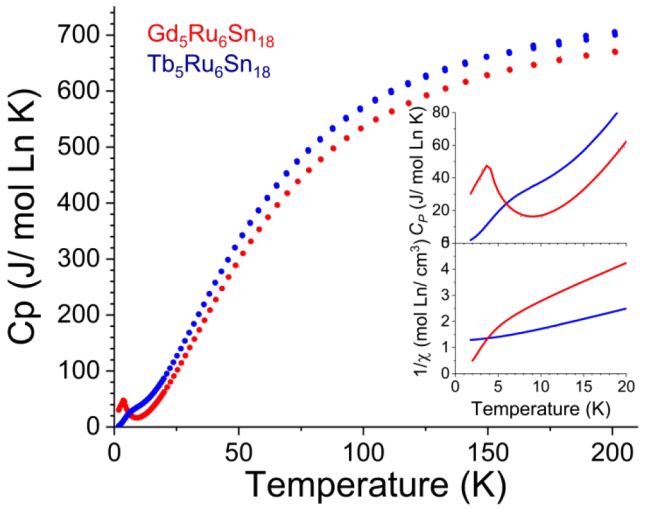

Figure 11. Heat capacity of $Ln_5Ru_6Sn_{18}$ (Ln = Gd, Tb) as a function of temperature. The inset contains a zoom-in of the heat capacity and the inverse magnetic susceptibility.

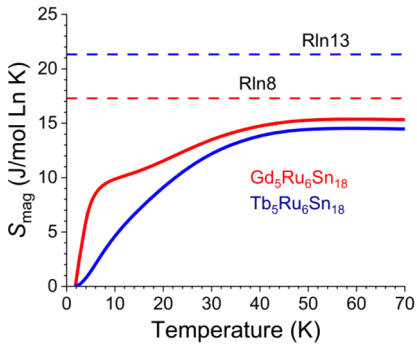

Figure 12. Magnetic entropy of $Gd_5Ru_6Sn_{18}$ (red) and $Tb_5Ru_6Sn_{18}$ (blue) with the corresponding theoretically expected value as the dashed lines.

susceptibility. Specific heat measurements of $Tb_5Ru_6Sn_{18}$ under larger magnetic fields reduce and shift the broad feature to higher temperatures until its disappearance at 9 T (Figure S8). The lack of thermal hysteresis in the magnetic susceptibility of $Tb_5Ru_6Sn_{18}$ rules out the presence of a spin glass transition. However, the observation that applying a larger magnetic field both suppresses the broad peak and shifts it to higher temperatures in the heat capacity, coinciding with the temperature at which a change in slope is observed in the inverse magnetic susceptibility (inset, Figure 11, blue), strongly suggests that this anomaly is associated with a phenomenon involving the magnetic degrees of freedom. To determine the magnetic contribution (C_{mag}) to the specific heat and the magnetic entropy (S_{mag}) of $Ln_5Ru_6Sn_{18}$ (Ln = Gd, Tb), we fit the heat capacity to a lattice-Debye model. The lattice-Debye fit $C_P = \gamma T + C_D(\frac{T}{\theta_D})^3 \int_0^{\theta_D/T} \frac{x^4 e^x}{(e^x-1)^2}$, where γ is the Sommerfeld coefficient, $x = h\omega/k_BT$, ω is the Debye frequency, θ_D is the Debye temperature, and C_D is a constant containing the number of oscillators and degrees of freedom. The lattice-Debye fit yields the Debye temperatures (θ_D) of 225 and 214 K and γ of 426 and 414 mJ/mol K^2 for the Gd and Tb analogues, respectively. When normalized to the number of Ln, γ is 85.2 and 82.8 mJ/mol Ln K^2. The Debye temperatures obtained for both analogues are close to the value obtained for the tetragonal $Sc_5Ru_6Sn_{18}$ (θ_D = 205 K); however, the Sommerfeld coefficients obtained are larger than the 36.93 mJ/mol K^2 reported for the tetragonal $Sc_5Ru_6Sn_{18}$.[43] We speculate that the large Sommerfeld reflects spin entropy even on the approach to zero temperature.

The C_{mag} to the heat capacity was determined by subtracting the lattice-Debye fit obtained between T = 50−200 K for the Gd and Tb analogues. The S_{mag} was obtained by integrating C_{mag}/T, as shown in Figure 12. For the Gd analogue, magnetic entropy increases rapidly around 5 K, coinciding with the change of slope observed in the inverse magnetic susceptibility, and steadily increases until it reaches a value of 15.3 J/mol Gd K (88% of R ln 8) at 50 K. The shortcoming of the entropy for the Gd analogue may be due to the release of magnetic entropy below 1.8 K. The S_{mag} for the Tb analogue steadily increases to around 50 K, where it saturates at 14.5 J/mol Tb K (68% of R ln 13). The lack of thermal hysteresis and the absence of sharp features in the magnetic susceptibility suggest short-range magnetic ordering is present in $Tb_5Ru_6Sn_{18}$. This is indicated by the reduction and shifting of the broad peak in heat capacity toward higher temperatures when a larger magnetic field is applied, as well as the steady increase in magnetic entropy observed well above the broad feature in heat capacity.

4. CONCLUSION

In this manuscript, we demonstrate the utility of tolerance maps in guiding the targeted growth of Remeika phases with the $Tb_5Rh_6Sn_{18}$ structure type, which have potential for exotic ground states induced by disorder. Specifically, the successful synthesis and characterization of $Ln_5Ru_6Sn_{18}$ (Ln = Gd, Tb) highlight the promise of incorporating a non-Kramers' ion (Tb^{3+}) as a platform for exploring intermetallic systems. The emergence of diffuse scattering features, supported by 3D-ΔPDF analysis, highlights the role of short-range, directional correlations among partially occupied Tb and Sn sites. These correlations may suppress long-range order and contribute to the lack of long-range magnetic transitions.

Magnetic susceptibility measurements indicated that neither analogue exhibited long-range magnetic ordering down to 1.8 K. The observed magnetic moment of 1.53 μ_B per cluster for $Tb_5Ru_6Sn_{18}$ at 1.8 K, along with a negative Curie−Weiss temperature and a broad feature in the heat capacity measurements, suggests the presence of short-range antiferromagnetic interactions, potentially among the Tb2 ions that form the regular tetrahedron. Furthermore, heat capacity measurements revealed a peak for the Gd analogue and a broad feature for the Tb analogue. Further investigation into the magnetic analogues that also adopt the cubic $Tb_5Rh_6Sn_{18}$ structure type is particularly promising because of the regular tetrahedral sublattice of rare-earth spins and the competing ferromagnetic and antiferromagnetic exchange interactions that may occur.

Our focus on the compound $Ln_5Ru_6Sn_{18}$ (where Ln = Gd or Tb) is driven by two main reasons: (i) its tolerance factor values (τ = 0.837 for Gd and τ = 0.844 for Tb), which place it close to the boundary between the $Yb_3Rh_4Sn_{13}$ and the $Er_5Rh_6Sn_{18}$/$Tb_5Rh_6Sn_{18}$ structure types (with τ = 0.83), and (ii) the potential for exotic ground states due to geometric frustration coupled with structural disorder. The observed structural disorder, geometric frustration, and diffuse scattering in diffraction experiments suggest that these features may underline the absence of long-range magnetic order in these compounds. This combination could enhance quantum

https://doi.org/10.1021/acs.chemmater.5c02568
Chem. Mater. 2025, 37, 9014−9024

fluctuations in non-Kramers' ions, such as Tb^{3+}, and warrants further investigation, especially at lower temperatures.

■ ASSOCIATED CONTENT

Data Availability Statement

Data will be made available upon request.

Supporting Information

The Supporting Information is available free of charge at https://pubs.acs.org/doi/10.1021/acs.chemmater.5c02568.

Figure S1: the structural relationship between Phases I–III; Figure S2: the graph mapping the $Ln_5Ru_6Sn_{18}$ (Ln = Gd, Tb) in the tolerance factor for Remeika phases; Figure S3: the powder X-ray diffraction of $Ln_5Ru_6Sn_{18}$ (Ln = Gd, Tb); Figure S4: a Laue backscattering image of $Tb_5Ru_6Sn_{18}$; Figure S5: the local environment of the Er1 cuboctahedral and the Sn1 tetrahedron in the $Er_5Rh_6Sn_{18}$ structure type; Figure S6: the $Er_5Rh_6Sn_{18}$ structure type emphasizing the distinct [$RhSn_6$] trigonal prisms and the Er2 tetrahedral arrangements; Figure S7: the Wohlfarth fit of the magnetization data of $Tb_5Ru_6Sn_{18}$; Figure S8: C/T vs T of $Tb_5Ru_6Sn_{18}$ under distinct applied fields (PDF)

Accession Codes

Deposition Numbers 2452673–2452674 contain the supplementary crystallographic data for this paper. These data can be obtained free of charge via the joint Cambridge Crystallographic Data Centre (CCDC) and Fachinformationszentrum Karlsruhe Access Structures service.

■ AUTHOR INFORMATION

Corresponding Author

Julia Y. Chan − *Department of Chemistry and Biochemistry, Baylor University, Waco, Texas 76798, United States;* orcid.org/0000-0003-4434-2160; Email: Julia_Chan@baylor.edu

Authors

Alexis Dominguez Montero − *Department of Chemistry and Biochemistry, Baylor University, Waco, Texas 76798, United States*

Gregory T. McCandless − *Department of Chemistry and Biochemistry, Baylor University, Waco, Texas 76798, United States*

Zachary J. Morgan − *Neutron Scattering Division, Oak Ridge National Laboratory, Oak Ridge, Tennessee 37831, United States*

Benny Schundelmier − *National High Magnetic Field Laboratory, Tallahassee, Florida 32310, United States; Department of Physics, Florida State University, Tallahassee, Florida 32306, United States;* orcid.org/0000-0002-7345-9977

Christina M. Hoffmann − *Neutron Scattering Division, Oak Ridge National Laboratory, Oak Ridge, Tennessee 37831, United States*

Ryan E. Baumbach − *Department of Physics, University of California, Santa Cruz, California 95064, United States*

Complete contact information is available at: https://pubs.acs.org/10.1021/acs.chemmater.5c02568

Notes

The authors declare no competing financial interest.

■ ACKNOWLEDGMENTS

J.Y.C. and A.D.M. acknowledge support from DOE-DE-SC0022854, as well as Welch AA-2056-20240404, for partial funding of this work. R.E.B. acknowledges support by the University of California, Santa Cruz through startup funds, as well as a portion of this work being performed at the National High Magnetic Field Laboratory, with the National Science Foundation Cooperative Agreement No. DMR-2128556 and the State of Florida support. This research was supported in part by an appointment to the Oak Ridge National Laboratory GRO Program, sponsored by the U.S. Department of Energy and administered by the Oak Ridge Institute for Science and Education. A portion of this research used resources at the Spallation Neutron Source, a DOE Office of Science User Facility operated by the Oak Ridge National Laboratory as part of the Graduate Research Program at ORNL. The beam time was allocated to POWGEN on proposal number IPTS-34807. B.S. acknowledges the support of the NHML User Collaboration Grant Program (UCGP). The authors acknowledge Dr. Kaya Wei and Dr. Feng Ye for their helpful discussions.

■ REFERENCES

(1) Handunkanda, S. U.; Curry, E. B.; Voronov, V.; Said, A. H.; Guzmán-Verri, G. G.; Brierley, R. T.; Littlewood, P. B.; Hancock, J. N. Large Isotropic Negative Thermal Expansion Above a Structural Quantum Phase Transition. *Phys. Rev. B* **2015**, *92*, 134101.

(2) Poudel, L.; Lawrence, J. M.; Wu, L. S.; Ehlers, G.; Qiu, Y.; May, A. F.; Ronning, F.; Lumsden, M. D.; Mandrus, D.; Christianson, A. D. Multicomponent Fluctuation Spectrum at the Quantum Critical Point in $CeCu_{6-x}Ag_x$. *npj Quantum Mater.* **2019**, *4*, 52.

(3) Ma, Z.; Dong, Z.-Y.; Wu, S.; Zhu, Y.; Bao, S.; Cai, Z.; Wang, W.; Shangguan, Y.; Wang, J.; Ran, K.; Yu, D.; Deng, G.; Mole, R. A.; Li, H.-F.; Yu, S.-L.; Li, J.-X.; Wen, J. Disorder-Induced Spin-Liquid-Like Behavior in Kagome-Lattice Compounds. *Phys. Rev. B* **2020**, *102*, 224415.

(4) Lei, S.; Duppel, V.; Lippmann, J. M.; Nuss, J.; Lotsch, B. V.; Schoop, L. M. Charge Density Waves and Magnetism in Topological Semimetal Candidates $GdSb_xTe_{2-x}$. *Adv. Quantum Technol.* **2019**, *2* (10), 1900045.

(5) Pollak, C. J.; Skorupskii, G.; Gutierrez-Amigo, M.; Singha, R.; Stiles, J. W.; Kamm, F.; Pielnhofer, F.; Ong, N. P.; Errea, I.; Vergniory, M. G.; Schoop, L. M. Chemical Bonding Induces One-Dimensional Physics in Bulk Crystal $BiIr_4Se_8$. *J. Am. Chem. Soc.* **2024**, *146*, 6784–6795.

(6) Kyrk, T. M.; Kennedy, E. R.; Galeano-Cabral, J.; McCandless, G. T.; Scott, M. C.; Baumbach, R. E.; Chan, J. Y. Much More to Explore with an Oxidation State of Nearly Four: Pr Valence Instability in Intermetallic *m*-$Pr_2Co_3Ge_5$. *Sci. Adv.* **2024**, *10*, eadl2818.

(7) Lai, Y.; Chan, J. Y.; Baumbach, R. E. Electronic Landscape of the *f*-Electron Intermetallics with the $ThCr_2Si_2$ Structure. *Sci. Adv.* **2022**, *8*, eabp8264.

(8) Dominguez Montero, A.; Stoian, S. A.; McCandless, G. T.; Baumbach, R. E.; Chan, J. Y. Role of $CeNiSi_2$ and $BaNiSn_3$ Structure Types in the Emergent Magnetism of the Homologous Series $Ln_{n+1}M_nX_{3n+1}$: $Ce_4Fe_3Ge_{10}$. *Chem. Mater.* **2024**, *36*, 8534–8545.

(9) Plata, M. A.; Smith, J. S.; Baumbach, R. E.; Strydom, A. M.; McCandless, G. T.; Chan, J. Y. Predicting Quantum Criticality in Single-Crystalline $Ce_2Ru_3Ge_5$. *Inorg. Chem.* **2025**, *64*, 12768–12780.

(10) Dominguez Montero, A.; McCandless, G. T.; Oladehin, O.; Baumbach, R. E.; Chan, J. Y. Development of a Geometric Descriptor for the Strategic Synthesis of Remeika Phases. *Chem. Mater.* **2023**, *35*, 2238–2247.

(11) Remeika, J. P.; Espinosa, G. P.; Cooper, A. S.; Barz, H.; Rowell, J. M.; McWhan, D. B.; Vandenberg, J. M.; Moncton, D. E.; Fisk, Z.; Woolf, L. D.; et al. A New Family of Ternary Intermetallic

Superconducting/Magnetic Stannides. *Solid State Commun.* **1980**, *34* (12), 923−926.
(12) Gui, X.; Lv, B.; Xie, W. Chemistry in Superconductors. *Chem. Rev.* **2021**, *121*, 2966−2991.
(13) Gumeniuk, R. Chapter 304 - Structural and Physical Properties of Remeika Phases, In *Handbook on the Physics and Chemistry of Rare Earths*, Bünzli, J.-C.-G.; Pecharsky, V. K. Eds.; Elsevier 2018, Vol. *54*, pp. 43−143.
(14) Oswald, I. W. H.; Rai, B. K.; McCandless, G. T.; Morosan, E.; Chan, J. Y. The Proof is in the Powder: Revealing Structural Peculiarities in the $Yb_3Rh_4Sn_{13}$ Structure Type. *CrystEngcomm* **2017**, *19*, 3381−3391.
(15) Iwasa, K.; Suyama, K.; Ohira-Kawamura, S.; Nakajima, K.; Raymond, S.; Steffens, P.; Yamada, A.; Matsuda, T. D.; Aoki, Y.; Kawasaki, I.; Fujimori, S.-I.; Yamagami, H.; Yokoyama, M. Weyl-Kondo Semimetal Behavior in the Chiral Structure Phase of $Ce_3Rh_4Sn_{13}$. *Phys. Rev. Mater.* **2023**, *7*, 014201.
(16) Hallas, A. M.; Huang, C. L.; Rai, B. K.; Weiland, A.; McCandless, G. T.; Chan, J. Y.; Beare, J.; Luke, G. M.; Morosan, E. Complex Transport and Magnetism in Inhomogeneous Mixed Valence $Ce_3Ir_4Ge_{13}$. *Phys. Rev. Mater.* **2019**, *3*, 114407.
(17) Gumeniuk, R.; Nicklas, M.; Akselrud, L.; Schnelle, W.; Schwarz, U.; Tsirlin, A. A.; Leithe-Jasper, A.; Grin, Y. $Y_3Pt_4Ge_{13}$: A Superconductor With a Noncentrosymmetric Crystal Structure. *Phys. Rev. B* **2013**, *87*, 224502.
(18) Fisk, Z.; Lambert, S. E.; Maple, M. B.; Remeika, J. P.; Espinosa, G. P.; Cooper, A. S.; Barz, H.; Oseroff, S. Magnetic and Superconducting Properties of Rare Earth Osmium Stannides. *Solid State Commun.* **1982**, *41* (1), 63−67.
(19) Bordet, P.; Miraglia, S.; Hodeau, J. L.; Marezio, M. Competition Between Magnetism and Superconductivity in Erbium Rhodium Stannide. *J. Solid State Chem.* **1999**, *147*, 399−409.
(20) Bhattacharyya, A.; Adroja, D.; Kase, N.; Hillier, A.; Akimitsu, J.; Strydom, A. Unconventional Superconductivity in $Y_5Rh_6Sn_{18}$ Probed by Muon Spin Relaxation. *Sci. Rep.* **2015**, *5*, 12926.
(21) Bhattacharyya, A.; Adroja, D. T.; Quintanilla, J.; Hillier, A. D.; Kase, N.; Strydom, A. M.; Akimitsu, J. Broken Time-Reversal Symmetry Probed by Muon Spin Relaxation in the Caged Type Superconductor $Lu_5Rh_6Sn_{18}$. *Phys. Rev. B* **2015**, *91*, 060503.
(22) Bhattacharyya, A.; Adroja, D. T.; Kase, N.; Hillier, A. D.; Strydom, A. M.; Akimitsu, J. Unconventional Superconductivity in the Cage-Type Compound $Sc_5Rh_6Sn_{18}$. *Phys. Rev. B* **2018**, *98*, 024511.
(23) Ślebarski, A.; Fijałkowski, M.; Maśka, M. M. Spin Fluctuations and Superconductivity in $Y_5Rh_6Sn_{18}$ Doped With Pd and Co: Evidence of Peak Effect in the Superconducting Mixed State. *Phys. Rev. B* **2022**, *106*, 075145.
(24) Wang, C.-W.; Karna, S. K.; Yano, S.-I.; Lee, C.-H.; Avdeev, M.; Lue, C. S.; Kuo, C. N. Magnetic Properties and Noncollinear Spin Structure of the Tin-Rich Stannide $Ho_5Co_6Sn_{18}$. *Phys. Rev. B* **2022**, *105*, 104429.
(25) Espinosa, G. P.; Cooper, A. S.; Barz, H. Isomorphs of the Superconducting/Magnetic Ternary Stannides. *Mater. Res. Bull.* **1982**, *17*, 963−969.
(26) Furukawa, T.; Miyagawa, K.; Itou, T.; Ito, M.; Taniguchi, H.; Saito, M.; Iguchi, S.; Sasaki, T.; Kanoda, K. Quantum Spin Liquid Emerging from Antiferromagnetic Order by Introducing Disorder. *Phys. Rev. Lett.* **2015**, *115*, 077001.
(27) Clark, L.; Sala, G.; Maharaj, D. D.; Stone, M. B.; Knight, K. S.; Telling, M. T. F.; Wang, X.; Xu, X.; Kim, J.; Li, Y.; Cheong, S.-W.; Gaulin, B. D. Two-Dimensional Spin Liquid Behaviour in the Triangular-Honeycomb Antiferromagnet $TbInO_3$. *Nat. Phys.* **2019**, *15*, 262−268.
(28) Canfield, P. C.; Fisk, Z. Growth of Single Crystals From Metallic Fluxes. *Philos. Mag. B* **1992**, *65*, 1117−1123.
(29) Krause, L.; Herbst-Irmer, R.; Sheldrick, G. M.; Stalke, D. Comparison of Silver and Molybdenum Microfocus X-ray Sources for Single-Crystal Structure Determination. *J. Appl. Crystallogr.* **2015**, *48*, 3−10.
(30) Sheldrick, G. M. SHELXT - Integrated Space-Group and Crystal-Structure Determination. *Acta Crystallogr., Sect. A* **2015**, *71*, 3−8.
(31) Sheldrick, G. M. Crystal Structure Refinement with SHELXL. *Acta Crystallogr., Sect. C* **2015**, *71*, 3−8.
(32) Schultz, A. J.; Jorgensen, M. R. V.; Wang, X.; Mikkelson, R. L.; Mikkelson, D. J.; Lynch, V. E.; Peterson, P. F.; Green, M. L.; Hoffmann, C. M. Integration of Neutron Time-of-Flight Single-Crystal Bragg Peaks in Reciprocal Space. *J. Appl. Crystallogr.* **2014**, *47*, 915−921.
(33) Arnold, O.; Bilheux, J. C.; Borreguero, J. M.; Buts, A.; Campbell, S. I.; Chapon, L.; Doucet, M.; Draper, N.; Ferraz Leal, R.; Gigg, M. A.; Lynch, V. E.; Markvardsen, A.; Mikkelson, D. J.; Mikkelson, R. L.; Miller, R.; Palmen, K.; Parker, P.; Passos, G.; Perring, T. G.; Peterson, P. F.; Ren, S.; Reuter, M. A.; Savici, A. T.; Taylor, J. W.; Taylor, R. J.; Tolchenov, R.; Zhou, W.; Zikovsky, J. Mantid—Data Analysis and Visualization Package for Neutron Scattering and μ SR Experiments. *Nucl. Instrum. Methods Phys. Res., Sect. A* **2014**, *764*, 156−166.
(34) Zikovsky, J.; Peterson, P. F.; Wang, X. P.; Frost, M.; Hoffmann, C. CrystalPlan: an Experiment-Planning Tool for Crystallography. *J. Appl. Crystallogr.* **2011**, *44*, 418−423.
(35) Michels-Clark, T. M.; Savici, A. T.; Lynch, V. E.; Wang, X.; Hoffmann, C. M. Expanding Lorentz and Spectrum Corrections to Large Volumes of Reciprocal Space for Single-Crystal Time-of-Flight Neutron Diffraction. *J. Appl. Crystallogr.* **2016**, *49*, 497−506.
(36) Hodeau, J. L.; Marezio, M.; Remeika, J. P. The Structure of $[Er(1)_{1-x}Sn(1)_x]Er(2)_4Rh_6Sn(2)_4Sn(3)_{12}Sn(4)_2$, a Ternary Reentrant Superconductor. *Acta Crystallogr., Sect. B* **1984**, *B40* (1), 26−38.
(37) Brown, W. K.; Schundelmier, B. C.; Tan, H.; Melnick, C.; Kotliar, G.; Yan, B.; Wei, K.; McCandless, G. T.; Chan, J. Y. $Sm_2Ru_3Sn_5$: A Noncentrosymmetric Cubic Member of the $Ln_2M_3X_5$ Family. *Z. Anorg. Allg. Chem.* **2025**, *651*, No. e202500021.
(38) Paddison, J. A. M.; Ross Stewart, J.; Goodwin, A. L. Spinvert: a Program for Refinement of Paramagnetic Diffuse Scattering Data. *J. Phys.: Condens. Matter* **2013**, *25*, 454220.
(39) Morgan, Z. J.; Zhou, H. D.; Chakoumakos, B. C.; Ye, F. RMC-Discord: Reverse Monte Carlo Refinement of Diffuse Scattering and Correlated Disorder from Single Crystals. *J. Appl. Crystallogr.* **2021**, *54*, 1867−1885.
(40) Weber, T.; Simonov, A. The Three-Dimensional Pair Distribution Function Analysis of Disordered Single Crystals: Basic Concepts. *Z. Kristallogr. - New Cryst. Struct.* **2012**, *227*, 238−247.
(41) Simonov, A.; Weber, T.; Steurer, W. Yell: a Computer Program for Diffuse Scattering Analysis Via Three-Dimensional Delta Pair Distribution Function Refinement. *J. Appl. Crystallogr.* **2014**, *47*, 1146−1152.
(42) Das, P. K.; Kumar, N.; Kulkarni, R.; Dhar, S. K.; Thamizhavel, A. Anisotropic Magnetic Properties and Superzone Gap Formation in CeGe Single Crystal. *J. Phys.: Condens. Matter* **2012**, *24*, 146003−146015.
(43) Kumar, D.; Kuo, C. N.; Astuti, F.; Shang, T.; Lee, M. K.; Lue, C. S.; Watanabe, I.; Barker, J. A. T.; Shiroka, T.; Chang, L. J. Nodeless Superconductivity in the Cage-Type Superconductor $Sc_5Ru_6Sn_{18}$ with Preserved Time-Reversal Symmetry. *J. Phys.: Condens. Matter* **2018**, *30*, 315803.

https://doi.org/10.1021/acs.chemmater.5c02568
Chem. Mater. 2025, 37, 9014−9024